

# The 2D pn Junction Driven Out-of-Equilibrium

Ferney A. Chaves, Pedro C. Feijoo and David Jiménez

*Departament d'Enginyeria Electrònica, Escola d'Enginyeria,  
Universitat Autònoma de Barcelona, Campus UAB, 08193 Bellaterra, Spain.*

## Abstract

Doped pn junctions are fundamental electrical components in modern electronics and optoelectronics. Due to the physical properties and unique structures of the two-dimensional (2D) materials, 2D pn junctions made of these novel materials may be considered as basic building blocks of more complex devices. In this work, we develop a comprehensive physics based simulator model to investigate the 2D lateral pn junction driven out-of-equilibrium based on the solution of the 2D Poisson's equation coupled to the drift-diffusion and continuity equations. Notably, the simulator takes into account the strong influence of the out-of-plane electric field through the surrounding dielectric. Our study reveals that a Shockley-like equation for the ideal current-voltage characteristic, similar to that of the 3D pn junction, can be obtained for 2D pn junctions, provided an appropriate effective depletion layer is defined. The impact of recombination-generation processes inside the large depletion layer produces significant deviation from current-voltage (J-V) characteristics. Moreover, we analyze the depletion and diffusion capacitances of 2D lateral pn junction and discuss its cut-off frequency as the relevant Figure-of-Merit (FoM) for RF applications. To investigate the impact of the dimensionality in the performance of 2D junctions, we benchmark the MoS<sub>2</sub> junction (2D case) against the Si junction (3D case).

## 1. Introduction

Two-dimensional (2D) layered materials like graphene, phosphorene and Transition metal dichalcogenides have encouraged researchers to develop a new generation of 2D crystal based electronic devices such as diodes, transistors, barristors and optoelectronic devices [1]–[7]. These devices can contain, as essential part of their structure, junctions consisting of these 2D layered materials, called 2D junctions. 2D junctions can be integrated into a device either by using an out-of-plane configuration, featuring vertically stacked Van der Waals-bounded layers [8], [9], or by lateral (in-plane) configuration, spanning adjacent regions of different doping in the covalently bounded 2D plane [10]–[12]. 2D lateral pn junctions are particularly useful for optoelectronic devices because the built-in potential created in the extended space charge region [13] separates and drives the photogenerated e-h pairs to generate photocurrent. While in the literature one can find many reports of experimental works on fabrication techniques and characterization of 2D junctions, the same is not

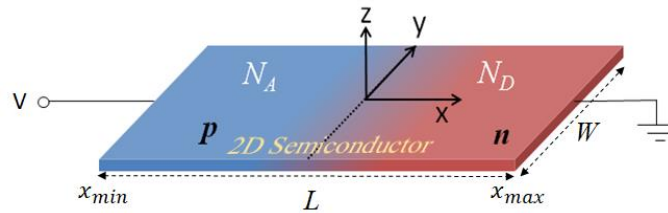


**Figure 1.** Scheme of the 2D lateral pn junction geometry

true for theoretical studies where the impact of the dimensionality on their electrical properties and their differences with the 3D junction (3DJ) are reported. Although some researchers have studied, from a theoretical point of view, the 2D lateral junction in equilibrium [14]–[17] the out-of-equilibrium regime remains to be investigated theoretically. Here, we report a study based on numerical simulations, which sets the basis to gain understanding of experimental measurements and for the assessment of future compact models. Our study have focused on the 2D lateral pn junction (2DJ), leaving for a future work the investigation of the 2D vertical pn junction. The manuscript has been divided in the following sections: in Section 2, we have described the numerical model used to investigate the properties of the 2DJ out-of-equilibrium; in Section 3 we have proposed a simple model describing the ideal electrical characteristics of 2DJ. Deviations from the ideality have also been discussed. In Section 4 we have investigated the impact of dimensionality on the J-V characteristics, specifically we have benchmarked the monolayer MoS<sub>2</sub> junction against the silicon junction. In Section 5, we have addressed the calculation of capacitances and conductance of 2DJ out-of-equilibrium. Based on these results, we have investigated its FoMs, such as the cut-off frequency. Finally, in Section 6 we have discussed the role played by the dielectric environment in defining the J-V characteristics and the possibility of tuning the diode rectification.

## 2. Numerical Model

Figure 1 represents the physical structure of the 2DJ considered in this work. The semiconductor lays in the plane  $z = 0$ , where there is an abrupt junction of p-type and n-type semiconductors at  $x = 0$ . The device width  $W$  along the y-axis is large enough to consider the independence of its properties on that direction. The metal electrodes at the edges of the device  $(x_{min}, y, 0)$  and  $(x_{max}, y, 0)$  are considered to make perfect ohmic contacts and supply a ground reference potential to the right edge and a potential  $V$  to the left edge. The non-linear Poisson's equation

$$-\nabla^2\phi(x, z; V) = \sigma(\phi; V)\delta(z)/\epsilon_{eff} \quad (1)$$

describes the 2DJ electrostatics, where  $\phi(x, z; V)$  is the 2D electrostatic potential distribution in the  $xz$ -plane when a bias  $V$  is applied to the device,  $\sigma$  is the sheet charge density,  $\epsilon_{eff}$  is the effective dielectric permittivity of the insulating media surrounding the junction and  $\delta(z)$  is the Dirac delta function. The effective permittivity  $\epsilon_{eff}$  is calculated as the mean value between the permittivity of the dielectric above the junction and the permittivity of the dielectric below the junction. The sheet charge density is  $\sigma = q(p - n + N_D - N_A)$ , where  $q$ ,  $n$  and  $p$  are the elementary charge, and the electron and hole sheet densities, respectively. By assuming complete ionization,  $N_D$  and  $N_A$  are the surface doping densities of donors and acceptors, respectively. Here, we have assumed chemically doped 2D semiconductors [5], while electrostatic doping will be the subject of future studies. Now, by integrating Eq. 1 along  $z$  and using the Dirac delta function properties, the electrostatic problem can be transformed into the following Laplace's equation:

$$\nabla^2\phi(x, z; V) = 0, \quad (2)$$

along with the boundary conditions:  $\partial\phi/\partial z = -\sigma(\phi)/2\epsilon_{eff}$  at  $z = 0$ , and Neumann-like boundary conditions for the rest of the domain boundaries, as shown in Figure 2, which illustrates the window of the numerical calculation. Additional details about the method to solve the Laplace's equation can be found in our previous work [14].

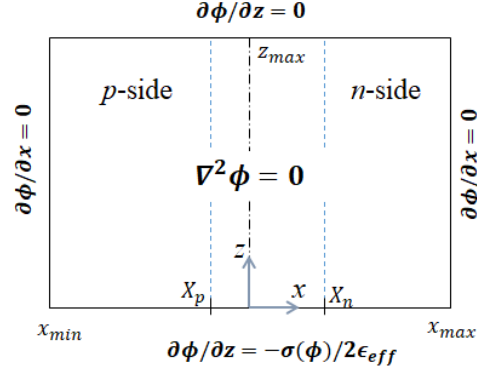


**Figure 2.** Calculation window of the 2D Poisson's equation and considered boundary conditions

For the description of the 2DJ electrostatics along the lateral dimension  $x$ , the drift and diffusion currents contributions must be considered for both electron and hole currents. Thus, the 1D electron and hole current densities are determined by the following equations:

$$J_n = -q\mu_n n \left[ \frac{d\phi}{dx} - \frac{D_n}{\mu_n n} \frac{dn}{dx} \right] = -q\mu_n n \frac{dV_n}{dx}, \quad (3a)$$

$$J_p = -q\mu_p p \left[ \frac{d\phi}{dx} + \frac{D_p}{\mu_p p} \frac{dp}{dx} \right] = -q\mu_p p \frac{dV_p}{dx}, \quad (3b)$$

where  $\mu_{n(p)}$  and  $D_{n(p)}$  are the electron (hole) mobility and diffusion coefficient, respectively,  $\phi(x) = \phi(x, 0; V)$  is the in-plane electrostatic potential under the quasi-steady state approximation and  $V_{n(p)}(x)$  is the electron (hole) quasi-Fermi potentials.  $\phi$  and  $V_{n(p)}$  are related to the local intrinsic energy  $E_i$  and electron (hole) Fermi energy as  $E_i(x) = -q\phi$  and  $E_{Fn(p)}(x) = -qV_{n(p)}$ , respectively. The boundary conditions set  $V_n$  and  $V_p$  to zero at the right edge of the n-side ( $x = x_{max}$ ) and  $V$  at the left edge of the p-side ( $x = x_{min}$ ). The local electron and hole densities can be written in terms of the electrostatic and the quasi-Fermi potentials as follow:

$$n(x) = n_s \log \left\{ 1 + e^{(q\phi(x) - qV_n(x) - E_g/2)/kT} \right\} \quad (4a)$$

$$p(x) = n_s \log \left\{ 1 + e^{(-q\phi(x) + qV_p(x) - E_g/2)/kT} \right\}, \quad (4b)$$

where  $n_s = g_{2D}kT$ , with  $g_{2D}$  the band-edge density of states (DOS),  $k$  the Boltzmann constant and  $T$  the absolute temperature [14]. As an example,  $g_{2D}$  for single layer MoS<sub>2</sub> is about  $5 \times 10^6 \text{eV}^{-1} \mu\text{m}^{-2}$  [18]. All the simulations in this work have been done assuming room temperature ( $T = 300 \text{K}$ ). Figure 3 shows the band diagram, Fermi energies and intrinsic energy profiles of a 2DJ, as calculated from our numerical model. In equilibrium a built-in potential  $\phi_{bi}$  develops across the depletion layer, while in the out-of-equilibrium regime it is reduced/augmented as  $\phi_{bi} - V$  according to the sign of  $V$ .

Finally, in order to complete our model we need to consider the conservation of the mobile charge through the continuity equations:

$$\frac{dJ_n}{dx} = qU(n, p) \quad (5a)$$

$$\frac{dJ_p}{dx} = -qU(n, p), \quad (5b)$$

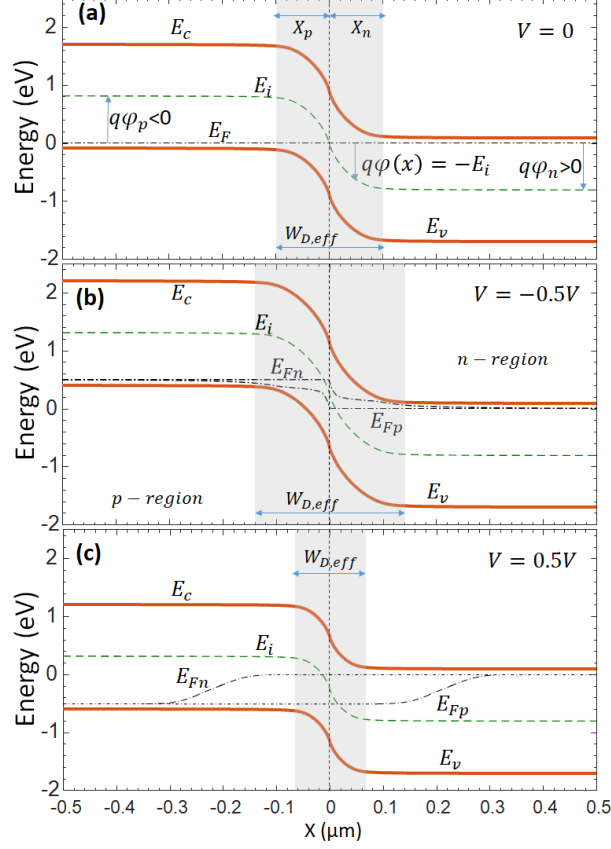


**Figure 3.** Band diagram of a 2D lateral pn junction in thermal equilibrium (a); reverse biased (b); and forward biased (c).

where  $U$  is the net recombination rate mediated by capture and emission of carriers at trap centers located in the band gap of the semiconductor. Note that, from Eqs. 5a-5b, then  $J(x) = J_n(x_0) + J_p(x_0) = J = const.$  Based on the Shockley-Red-Hall model, like in 3D semiconductors [19], the following expression for  $U$  can be obtained (for the non-degenerated case):

$$U = \frac{pn - n_i^2}{\tau_p(n + n_i) + \tau_n(p + n_i)} \quad (6)$$

where  $\tau_{n(p)}$  represents the minority electron (hole) lifetime, at low-level injection, and  $n_i = n_s \log[1 + \exp(-E_g/2kT)]$  is the 2D intrinsic electron density.

Our method solves Eqs. 2-5 in a self-consistent way in order to get  $\phi(x, z)$ ,  $V_n(x)$ ,  $V_p(x)$ ,  $J_n(x)$ ,  $J_p(x)$  for a given applied bias  $V$ . Appendix 1 details the algorithm used to solve the abovementioned set of equations.

### 3. The ideal 2D diode

Similarly to conventional 3D pn junctions, it is possible to obtain an analytical model (the equivalent to Shockley's equation) for the ideal 2DJ. For 3DJ the following approximations are assumed so to develop the ideal model [19], [20]: (i) A dipole layer fully depleted of carriers with abrupt boundaries supports the voltage drop  $\varphi_{bi} - V$  and, outside those boundaries, the semiconductor is assumed to be neutral. (ii) The carrier statistics is assumed to follow a Boltzmann distribution, implying that the

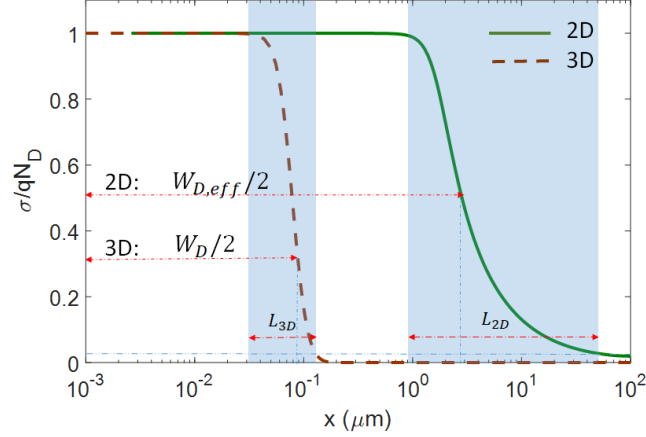


**Figure 4.** Charge density profile for symmetric 2D and 3D lateral pn junctions, showing the depletion region and transition region for both cases. Only n-side region is shown.

semiconductor is assumed to be non-degenerated. (iii) The excess of minority carriers injected in the quasi-neutral region is much less than the corresponding majority carrier density (low injection approximation). (iv) There is a zero net recombination rate ( $U = 0$ ) inside the depletion layer such that the total current is only due to the diffusion component of minority carriers in the neutral regions.

In this Section, we discuss the possibility of extending the previous assumptions to 2DJs in order to get the 2D equivalent to the Shockley equation. This will be done on the basis of numerical simulations relying on the model described in Section 2.

Figure 4 shows, from our simulations, the normalized charge density along the n-side of symmetric 2DJ and 3DJ devices in thermal equilibrium. These devices have similar parameters which correspond to 2DJ1 and 3DJ1 described in Table I, except for their corresponding DOS. Remarkably, the semiconductor of 2DJ1 device has a gap of energy similar to that of Si and equivalent doping characterized by the energies  $q\phi_n$  and  $q\phi_p$  represented in Figure 3a, i.e.  $\phi_{n,2D} = \phi_{n,3D} = |\phi_{p,2D}| = |\phi_{p,3D}|$ . In Figure 4, the shaded regions represent the transition regions between the fully depleted layer ( $\sigma/qN_D \sim 1$ ) and the quasi-neutral region ( $\sigma/qN_D \sim 0$ ) for both devices. It is worth noticing that we have used the notation  $\sigma$  and  $N_D$  for both 2D case and 3D case. That is,  $\sigma$  and  $N_D$  represent surface (volume) charge density and surface (volume) doping density in the 2D (3D) case, respectively. The length of the transition regions are  $L_{2D} \sim 48 \mu\text{m}$  and  $L_{3D} \sim 0.1 \mu\text{m}$  for the examined 2DJ and 3DJ, respectively. It is worth noticing that the 2D transition region is much wider ( $\sim 500\times$  for the examined case) than the 3D case because of a weaker screening of charge carriers related with a significant out-of-plane electric field, as compared with the strong screening exhibited in 3DJs. The strong screening in 3DJs justifies the total depletion approximation, giving place to a well-defined depletion region of width:

$$W_D = \sqrt{\frac{4\epsilon(\phi_{bi}-V)}{qN}}, \quad (7)$$

where  $N = N_A = N_D$  for the symmetric junction. As for the 2DJ, there also exists a depletion layer which width has been modeled in Ref. [17], by using a method based on infinite number of reflections of the image charge, which have resulted in:

$$W_{D,eff(1)} = \frac{\pi^2 \epsilon_{eff} (\phi_{bi}-V)}{4GqN} \quad \text{Symmetric case,} \quad (8a)$$

$$W_{D,eff(1)} = \frac{\pi^2 \epsilon_{eff} (\phi_{bi} - V)}{qN_D (7.12 \log_{10} \left( \frac{N_A}{N_D} \right) + 2.01)} \quad \text{Asymmetric } p^+n \text{ case, (8b)}$$

where  $G = 0.915$  is the Catalan's constant. However, Eq. 8b is not as accurate as Eq. 8a resulting in non-negligible electric field at the edges of the depletion layer. A more appropriate  $W_{D,eff(2)}$  could be defined, numerically determined by the condition  $\sigma/qN = 56.4\%$  at both sides of the junction, guaranteeing an almost zero field at the edges. This ratio guarantees that for symmetric 2DJs both definitions  $W_{D,eff(1)}$  and  $W_{D,eff(2)}$  give the same result. Once defined the EDL, it is possible to consider the 2DJ as consisting of three regions as in 3DJs: the quasi-neutral  $p$ -side, the quasi-neutral  $n$ -side, and the EDL. Now, by assuming zero net recombination ( $U = 0$ ) inside the EDL, low injection, and the Boltzmann approximation to calculate the carrier densities, a Shockley-like equation for the ideal 2DJ case can be obtained. Although not shown here, the 2D Shockley-like equation comes, in total analogy with the 3D case, from the solution of the continuity equation to get the diffusion current of the minority carriers  $J_{n(p)}$  in the quasi-neutral regions [20], which allows to get the total current ( $J_{Ideal}$ ) density for a given bias as:

$$J_{Ideal} = J_p + J_n = J_o \left[ e^{\frac{qV}{kT}} - 1 \right], \quad (9)$$

where

$$J_o = qn_i^2 \left[ \frac{D_p}{L_p N_D} + \frac{D_n}{L_n N_A} \right] \quad (10)$$

is the reverse saturation current density per unit length, and the electron (hole) diffusion length is defined as  $L_{n(p)} \equiv \sqrt{D_{n(p)} \tau_{n(p)}}$ . Assuming non-degenerated 2D semiconductors, Eq. 4 reduces to:

$$n = n_i \exp \left[ \frac{q(\phi - V_n)}{kT} \right] \quad (11a)$$

$$p = n_i \exp \left[ \frac{q(V_p - \phi)}{kT} \right] \quad (11b)$$

where  $n_i = n_s \exp(-E_g/2kT)$ . On the other hand, for the non-degenerated case, the diffusion coefficient  $D_{n(p)}$  becomes  $D_{n(p)} = kT \mu_{n(p)}/q$ . For 2D semiconductor crystals  $n_i$  is typically much smaller than  $10^{11} \text{cm}^{-2}$  of zero-gap graphene. For example, monolayer  $\text{MoS}_2$  and  $\text{MoTe}_2$  semiconductors, with gaps of 1.8 eV and 1.15 eV, respectively, have intrinsic carrier densities  $\sim 10^{-2} \text{cm}^{-2}$  and  $\sim 10^3 \text{cm}^{-2}$ , respectively.

Next, the ideal 2D diode equation has been benchmarked against numerical simulations based on Eqs. 2-5 assuming  $U = 0$  inside the EDL. Figure 5a presents the results for the symmetric case. The

Device	Description	$E_g$ (eV)	$\epsilon_{eff}/\epsilon_0$	$n_i$ ( $\text{cm}^{-2}$ )	$\mu_p$ ( $\text{cm}^2/\text{Vs}$ )	$\mu_n$ ( $\text{cm}^2/\text{Vs}$ )	$\tau_p$ (s)	$\tau_n$ (s)	$\phi_p$ (eV)	$\phi_n$ (eV)
2DJ1	Sym. pn Small gap	1.12	11.9	5E3	280	350	1E-6	2E-7	0.4	0.4
2DJ2	Asym. p <sup>+</sup> n Large gap ( SL MoS <sub>2</sub> )	1.8	3.9	9.9E-3	50	50	3E-10	3E-10	0.89	0.81
2DJ3	Sym. pn Large gap (SL MoS <sub>2</sub> )	1.8	3.9	9.9E-3	50	50	3E-10	3E-10	0.81	0.81
3DJ1	Sym. pn Low doping (Si)	1.12	11.9	1.4E10	280	350	1E-6	2E-7	0.4	0.4
3DJ2	Sym. pn High doping (Si)	1.12	11.9	1.4E10	280	350	1E-6	2E-7	0.47	0.47
3DJ3	Asym. p <sup>+</sup> n (Si)	1.12	11.9	1.4E10	350	350	2E-7	2E-7	0.55	0.47

**Table I.** Parameters used in our simulations. SL: Single Layer

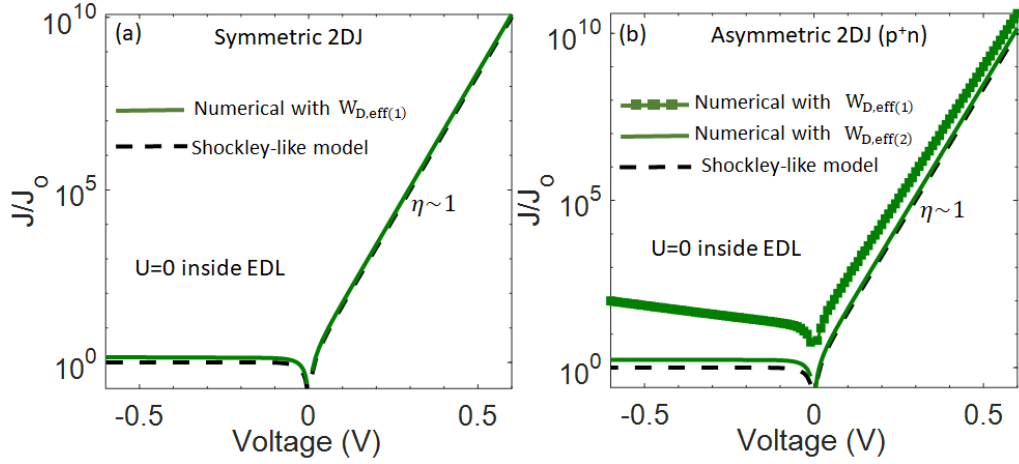


**Figure 5.** Ideal J-V characteristics of 2D lateral pn junction. (a) Symmetric 2DJ1 device.  $W_{D,eff(1)}$  has been calculated according to Eq. 8a. (b) Asymmetric 2DJ2 device.  $W_{D,eff(1)}$  has been calculated according to Eq. 8b and  $W_{D,eff(2)}$  according to the criterion  $\sigma/qN \sim 0.56$ . In both cases a zero net recombination rate ( $U = 0$ ) has been assumed inside the EDL.

parameters here used correspond to the device 2DJ1 described in Table I. As can be observed from the figure, the 2D Shockley-like equation (ideality factor  $\eta = 1$ ), fits very well with the numerical simulation at both reverse and forward polarizations even when not strictly applicable the full depletion approximation. On the other hand, Figure 5b shows the ideal J-V characteristics together with the numerical simulations for an asymmetric 2D  $p^+n$  junction with parameters described by device 2DJ2 in Table I. Again, the black dashed curve has been calculated with the Shockley-like equation with  $J_o = 2.9 \times 10^{-30}$  A/cm and the other are from the numerical model with the two different definitions given for  $W_{D,eff}$ . Importantly, the 2D Shockley-like equation fits much better the numerical simulation taking  $W_{D,eff(2)}$  as the effective depletion layer width rather than  $W_{D,eff(1)}$ .

Next, we have analyzed in more detail the electrostatics of asymmetric 2DJ. Figure 6a shows the relative total charge density calculated at forward bias, for asymmetric 2DJ as a function of the position. The asymmetric 3DJ case is also shown for comparison purposes. The parameters here used are those of the 2DJ2 and 3DJ3 devices in Table I. It is clear that the widths  $W_{D,eff(1)}$  and  $W_{D,eff(2)}$  are quite different. The reason why  $W_{D,eff(2)}$  results in a better fit of the Shockley model with the numerical model can be understood by means of Figure 6b, which shows the electrostatic potential along the device. At  $W_{D,eff(2)}$  the electric field is much closer to zero than for  $W_{D,eff(1)}$ , so the beginning of the quasi-neutral region is better defined with  $W_{D,eff(2)}$ . Figure 6c shows that the electric field for the 2D case is not linear with the position, as in the 3D case, but it goes as  $\ln(x/(x - X_n))$  near the junction. Finally, Figure 6d shows the carrier density profiles  $n(x)$  and  $p(x)$  of the 2DJ2 device at equilibrium and out-of-equilibrium. In the inset, we have repeated the carrier density profiles at forward bias ( $V = 0.5V$ ) in a wider region, exhibiting a constant slope (in logarithmic scale) in the quasi-neutral region, near the edge of the EDL, related with the hole diffusion length  $L_p$ . The extracted

value of  $L_p$  is  $\sim 0.19\mu\text{m}$  which coincides with  $L_p \equiv \sqrt{kT\mu_p\tau_p/q}$ , as expected from the parameters of 2DJ2 device in Table I.

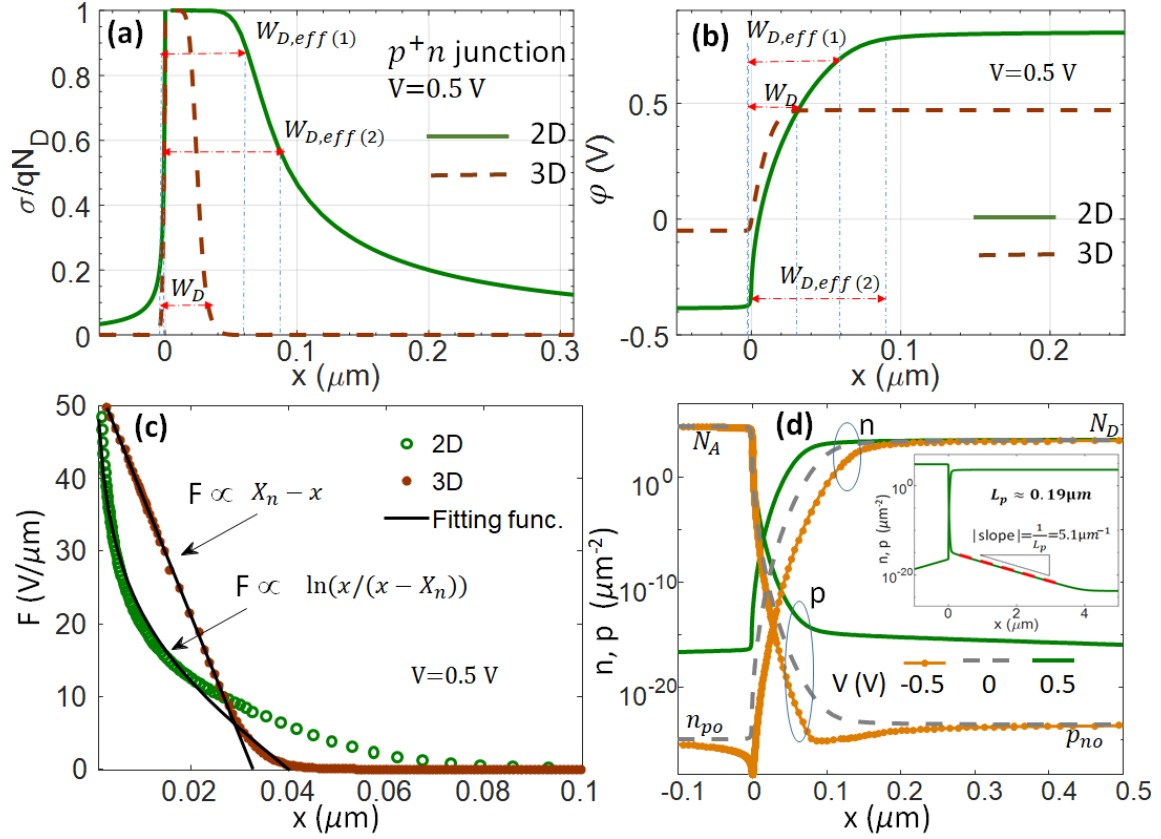


**Figure 6.** Electrostatic properties of asymmetric 2D lateral pn junction. (a) Normalized total charge; (b) Electrostatic potential; (c) Electric field; (d) Carrier density ( $p$  and  $n$ ) in the 2DJ at equilibrium, forward and reverse bias. Inset: numerical extraction of the hole diffusion length. The asymmetric 3DJ case is also shown in (a), (b) and (c) for comparison purposes.

#### 4. Impact of the dimensionality in 2D lateral pn junctions.

In order to investigate the impact of the dimensionality in 2DJs, we have carried out simulations of both symmetric 2DJ and 3DJ with similar parameters as given by devices 2DJ1 and 3DJ1, respectively, except by their DOS. We have taken into account R-G processes inside the EDL. The devices have been simulated up to forward biases such that the series resistance of the quasi-neutral regions can be appreciated. The resulting current densities are shown in Figure 7, normalized to the corresponding  $J_o$ . In the main panel, marked as “Ideal”, are the J-V characteristics with  $U = 0$  inside the EDL defined by  $W_D$  and  $W_{D,eff}$  in Eqs. 7 and 8a, respectively. The “Ideal” curves fit the Shockley equation  $J = J_o(e^{qV/\eta kT} - 1)$ , with ideality factor  $\eta = 1$ , quite well within the voltage range where no appreciable influence of series resistance is observed. More specifically, as shown in the inset, the ideality factor extracted from the numerical results is  $\sim 1$  up to  $V \sim 0.7\text{V}$  for the “Ideal” case, and then it quickly increases. On the other hand, the “Non-ideal” curves are obtained after considering  $U \neq 0$  inside the EDL according to Eq. 6. Different regions of J-V characteristics can be observed depending on the bias, namely: generation current (G) at reverse bias, recombination current (R) at low forward bias,

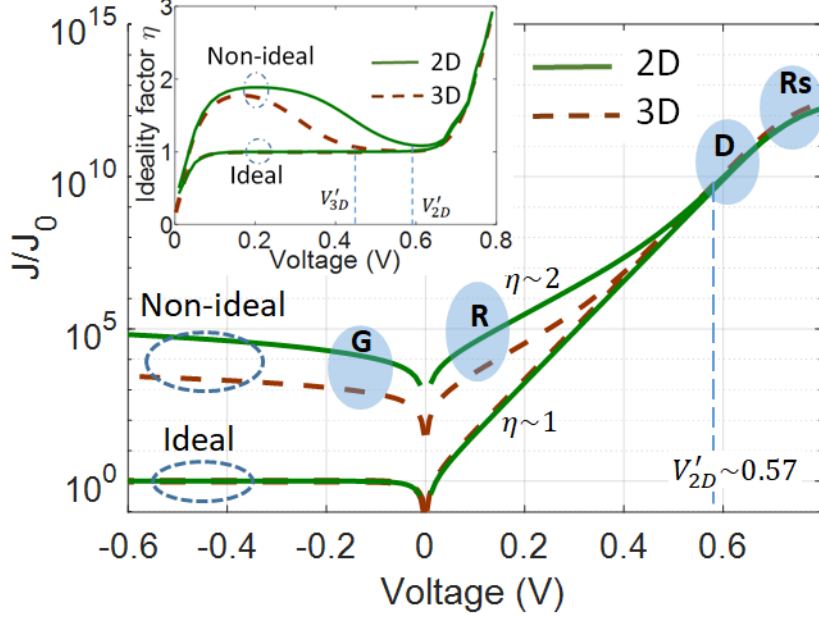


**Figure 7.** J-V characteristics for symmetric 2D and 3D lateral pn junctions showing the different components of the current. Inset: Ideality factor vs V. Labels “G”, “R”, “D” and “Rs” correspond to the region dominated by generation current, recombination current, diffusion current and current driven by series resistance, respectively.

diffusion current (D) at moderate forward bias, and current dominated by the series resistance (Rs) at high forward bias. High injection conditions are not present within the considered voltage range. Clearly, some differences between the 2D and 3D cases appear, even though the used parameters are similar. In the main figure, at reverse bias, the relative current density of the 2DJ is larger than the 3DJ. To understand this result, let us consider, firstly, the current driven by R-G processes under reverse-bias. Inside the EDL  $p \ll n_i$ ,  $n \ll n_i$ , so  $U < 0$  is then dominated by generation of electron-hole pairs, and can be expressed as:

$$U \approx -\frac{n_i^2}{n_i\{\tau_p(1+\frac{n}{n_i})+\tau_n(1+\frac{p}{n_i})\}} \cong -\frac{n_i}{\tau_g}, \quad (12)$$

where  $\tau_g$  is the generation lifetime, defined by the expression in brackets. The current due to generation in the effective depletion region can be roughly estimated by assuming a mean value  $\bar{U} = -n_i/\bar{\tau}_g$  of net recombination inside the EDL as:

$$J_G = \int_{-x_p}^{x_n} q |\bar{U}| dx \approx \frac{qn_i W_{D,eff}}{\bar{\tau}_g} \quad (13)$$

Figure 8 shows the profiles of  $U$  for a 2DJ at both reverse and forward bias, obtained from our numerical model, along with  $|\bar{U}|$  in the EDL with  $\bar{\tau}_g \sim \tau_p \sim \tau_n$ . Thus, the ratio  $J_G/J_0$  can be written as:

$$\frac{J_G}{J_0} \propto \frac{N_D}{n_i} \frac{W_{D,eff}}{(L_p+L_n)}. \quad (14)$$

This result is also valid for 3DJ after changing  $W_{D,eff}$  by  $W_D$ . Typically,  $W_{D,eff}$  for 2DJs is larger than  $W_D$  in 3DJs because of the weaker screening of charge carriers in 2D. On the other hand,  $L_p$  and  $L_n$

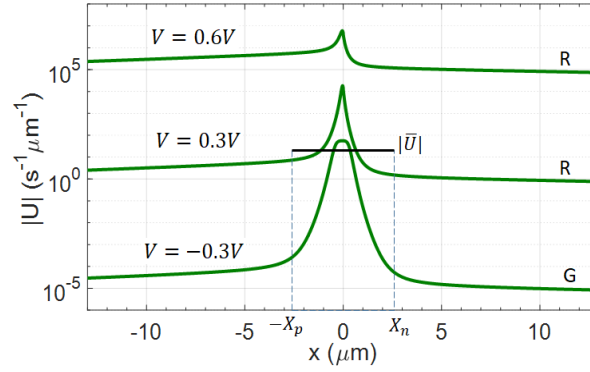


**Figure 8.** Net recombination rate profile at reverse bias ( $V = -0.3 V$ ) and forward bias ( $V = 0.3 V$  and  $0.6 V$ ).

are typically smaller in 2D as a consequence of smaller lifetimes and mobilities. Assuming the same  $N_D/n_i$  for the 2D and 3D, it does result in a larger  $J_G/J_o$  for the 2D case.

On the other hand, at forward bias, the major R-G processes in the EDL are the electron and hole capture processes (recombination) from the conduction and valence band, respectively, into the trap centers in the bandgap. Thus, a net recombination rate  $U > 0$  produces a dominant recombination current (R) over the diffusion current (D) in the quasi-neutral regions. This is valid from zero bias up to the crossover voltage  $V'_{2D}$  reached when  $J_R/J_{ideal} \sim 1$  (see Fig. 7). By following the same procedure that in the literature for 3D pn junctions, it is possible to find a simple expression for the recombination current density  $J_R$  at  $V > kT/q$  [21]:

$$J_R = \sqrt{\frac{\pi}{2}} \frac{kT n_i}{\tau F_o} \exp\left(\frac{qV}{2kT}\right), \quad (15)$$

where  $F_o$  is the electric field at the location of maximum recombination and a characteristic ideality factor  $\eta = 2$  is present. To get this expression for  $J_R$  we have assumed  $\tau_p = \tau_n = \tau$  for simplicity. As shown in Figure 6c, the dependence of the electric field for 2DJ with the position is not as simple as the 3D case and, in general, numerical approximations are needed to find  $F_o$  as a function of the applied voltage. However, by using the simple approximation  $F_o \approx \bar{F} = \frac{\phi_{bi} - V}{W_{D,eff}}$ , which is the average electric field in the EDL, a bias independent formula  $F_o = \frac{4GqN_D}{\pi^2 \epsilon_{eff}}$ , valid for symmetric junctions, can be obtained. Thus, the ratio  $J_R/J_{ideal}$  at forward bias results in:

$$\frac{J_R}{J_{ideal}} \approx \sqrt{\frac{\pi}{2}} \frac{kT}{q} \frac{\pi^2 \epsilon_{eff}}{8Gq n_i L_p} \exp\left(-\frac{qV}{2kT}\right). \quad (16)$$

Again, this ratio is typically larger for 2DJs than for 3DJs due to the lower intrinsic carrier densities, carrier lifetimes and mobilities for the 2D semiconductors. In addition, a closed expression for the crossover voltage  $V'_{2D}$ , can be obtained:

$$V'_{2D} \approx \frac{2kT}{q} \log\left(\sqrt{\frac{\pi}{2}} \frac{kT}{q} \frac{\pi^2 \epsilon_{eff}}{8Gq n_i L_p}\right). \quad (17)$$

Using the parameters for the device 2DJ1 in Table I,  $V'_{2D} \sim 0.57 V$ , which agrees with the obtained value in Figure 7 from our numerical model. The value of  $V'_{3D}$  cannot be analytically obtained, but from

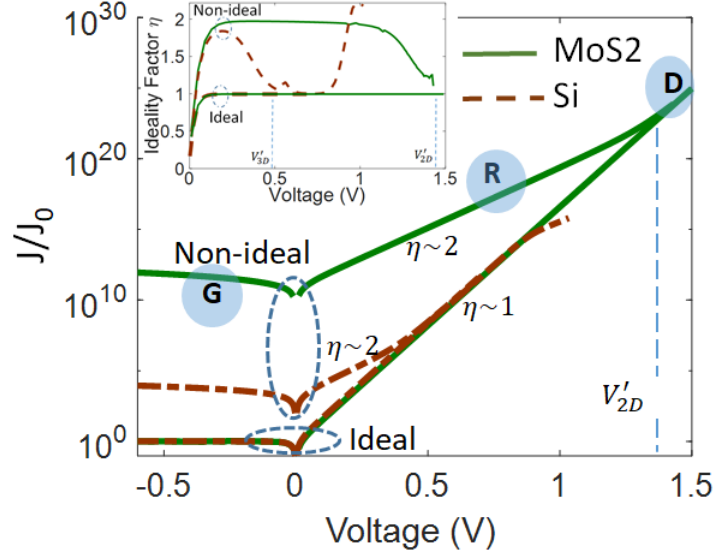


**Figure 9.** J-V characteristics of symmetric pn junctions: MoS<sub>2</sub> junction (2D case), Si junction (3D case). Inset: ideality factor vs voltage.

our simulation  $V'_{3D} \sim 0.42$  V, as illustrated in the inset of Figure 7. These effects can also be understood through the difference between their EDL in thermal equilibrium with  $W_{D,eff} = 5.24 \mu\text{m}$  and  $W_D = 0.17 \mu\text{m}$  for 2DJ and 3DJ, respectively.

Now, let's examine the differences between a typical 3DJ made of Si and a 2DJ made of monolayer MoS<sub>2</sub>. For this, we have simulated symmetric devices 2DJ3 and 3DJ2 described in Table I. For the sake of making a fair comparison the selected doping in each device is such that  $(E_F - E_V)|_{2D} = (E_F - E_V)|_{3D} = (E_c - E_F)|_{2D} = (E_c - E_F)|_{3D}$  is fulfilled the quasi-neutral region, far away from the EDL. Numerical results of the normalized J-V characteristics are shown in Figure 9. We can observe that  $J_G/J_0$  for the 2DJ is  $\sim 10^8$  larger than the 3D one, and the crossover voltage  $V'_{2D}$  for the 2D pn junction is approx. 1 V larger than  $V'_{3D}$ . Again, this can be understood because of the drastic reduction of both the intrinsic carrier density and diffusion length of minority carriers (smaller lifetimes and mobilities) together with the larger EDL in the 2D case. As for the 2D case the  $R_s$ -effect is not visible within the considered voltage range. However, for the 3DJ the  $R_s$ -effect starts to be strong at  $\sim 0.8$  V. Remarkably, the MoS<sub>2</sub> 2DJ exhibits an ideality factor close to 2 up to  $\sim 1.3$  V, indicating the dominance of the recombination current over the diffusion current. Interestingly, experimental evidence of this phenomenon, has been reported by Choi et al. [5] for 7nm thick MoS<sub>2</sub> lateral pn junctions and Baugher et. al [22] for electrically tunable pn diodes. Their experimental evidence reveals that the thinner the crystal semiconductors the nearer to 2 the ideality factor.

## 5. Capacitances and cut-off frequency in 2D lateral pn junctions.

In this section we address the investigation of the capacitances associated to the 2DJ in the out-of-equilibrium regime. An equivalent circuit will be presented and the cut-off frequency of the 2DJ will be analyzed. For the sake of simplicity, we have focused the discussion on the symmetric 2DJ. Let us begin discussing the depletion-layer capacitance per unit length, defined as  $C_{dp} = dQ_D/dV$ , where  $dQ_D$  is the incremental depletion charge on each side of the junction after applying an incremental

voltage change  $dV$ . Assuming the total depletion approximation, the depletion charge on the p-side, for example, can be calculated as  $Q_D = -qNW_{D,eff}(V)/2$ . From Eq. 8a we can obtain:

$$C_{dp} = \frac{\pi^2 \epsilon_{eff}}{8G}, \quad (18)$$

which does not depend on the applied voltage, in striking contrast to the 3D case. The depletion-layer capacitance accounts for most of the junction capacitance when the junction is reverse-biased. At forward bias, a diffusion capacitance exists in addition to the depletion capacitance. The diffusion capacitance is the result of the rearrangement of minority surface carrier in the quasi-neutral regions. Thus, in a similar way to the 3D case, when a small ac signal, characterized by an angular frequency  $\omega$ , is applied to a 2DJ that is forward-biased at a dc voltage  $V$ , the total voltage and current can be written as:

$$V^*(t) = V + v^* \exp(i\omega t) \quad (19)$$

$$J^*(t) = J + j^* \exp(i\omega t) \quad (20)$$

where  $v^*$  and  $j^*$  are the small-signal voltage and current density, respectively. The real and imaginary parts of the admittance  $j^*/v^*$  are related with the diffusion conductance  $G_d$  and diffusion capacitance  $C_{df}$ , respectively. By applying the same procedure as the one used for 3DJs [20], the following expressions for the low frequency diffusion capacitance and conductance, respectively, are obtained:

$$C_{df} = \frac{q^2 n_i^2 (L_p + L_n)}{2kTN} \exp\left(\frac{qV}{kT}\right), \quad (21)$$

and

$$G_d = \frac{q^2 n_i^2}{kTN} \left( \frac{D_p}{L_p} + \frac{D_n}{L_n} \right) \exp\left(\frac{qV}{kT}\right), \quad (22)$$

which is the same result as the one that can be obtained by differentiating Eq. 9, that is  $G_d = dJ_{ideal}/dV = r_d^{-1}$ , where  $r_d$  is defined as the differential resistance. In Figure 10 we have shown the behavior of both  $C_{dp}$  and  $C_{df}$  capacitances as a function of  $V$  for 2DJ1 with small gap (Fig. 10a) and

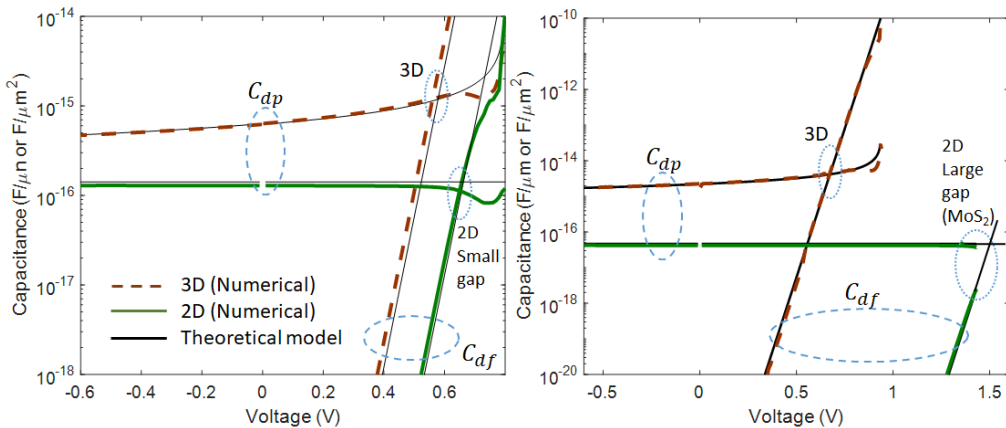


**Figure 10.** Depletion and diffusion capacitances of 2D lateral pn junction and comparison with the 3D case. (a) Small gap case, represented by devices 2DJ1 and 3DJ1. (b) Large gap case, represented by devices 2DJ3 and 3DJ2.

2DJ3 with large gap (Fig. 10b). More details of those devices are given in Table I. The green solid lines correspond to the capacitances obtained from our numerical model, according to:

$$C_{dp} = \frac{d}{dV} \int_0^{W_{D,eff}/2} q\sigma(x)dx, \quad (23)$$

and

$$C_{df} = \frac{d}{dV} \int_{x_{min}}^{-W_{D,eff}/2} q\Delta n(x) dx + \frac{d}{dV} \int_{W_{D,eff}/2}^{x_{max}} q\Delta p(x) dx, \quad (24)$$

where  $\Delta p(x)$  and  $\Delta n(x)$  are the excess of hole and electron surface densities, respectively, in the quasi-neutral regions. The black solid lines refer to the theoretical model, where the  $C_{dp}$  and  $C_{df}$  capacitances have been calculated from Eqs. 18 and 21, respectively. In Figure 10 we have included the corresponding 3D simulations and theoretical model outcome from [20] for comparison purposes (brown dashed lines). The 2D and 3D capacitances have units of  $F/\mu\text{m}$  and  $F/\mu\text{m}^2$ , respectively. Importantly, Eqs. 18 and 21 fit very well to the numerical result, both in 2D and 3D cases.

By taking advantage of the  $C_{dp}$  insensitivity to the voltage, a simple formula for the critical bias  $V^*$  that makes  $C_{dp} \cong C_{df}$ , can be obtained:

$$V^* = \frac{kT}{q} \log \left( \frac{kT \pi^2 \epsilon_{eff} N}{q^2 4Gn_i^2 (L_p + L_D)} \right) \quad (25)$$

For the examined devices 2DJ1 and 2DJ3, the calculated critical voltages are  $\sim 0.66$  V and  $\sim 1.5$  V, respectively. These values agree with the numerical results shown in Figure 10. In general, 2DJs made of large gap semiconductors with both low carrier lifetimes and mobilities exhibit a relatively high critical voltage  $V^*$ , resulting in a total capacitance  $C_T$  dominated by the depletion component, that is  $C_T = C_{dp} + C_{df} \sim C_{dp}$  that, interestingly, could be modulated by the dielectric permittivity of the surrounding media, according to Eq. 18.

The equivalent circuit model of the diode can be obtained as the total capacitance  $C_T$ , in parallel with its ac differential resistance  $r_d$ . The resistance of the quasi-neutral regions and contact resistance can be modeled by a resistance  $R_s$  in series with the parallel combination of  $C_T - r_d$  as shown in the inset

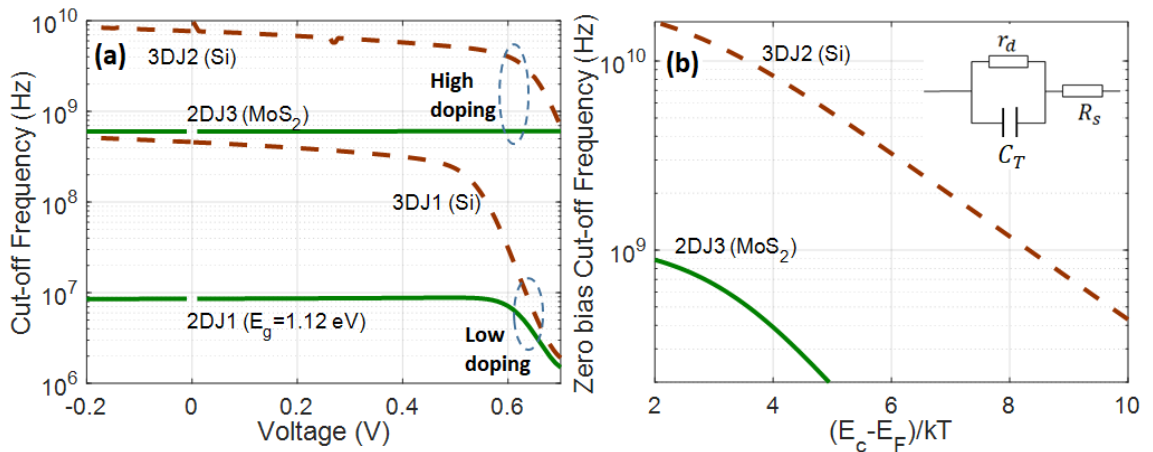


**Figure 11.** (a) Cut-off frequency as a function of the dc bias for 2DJ and 3DJ devices. (b) Zero bias cut-off frequency as a function of the doping for 2DJ (MoS<sub>2</sub>) and 3DJ (Si) devices, represented by 2DJ3 and 3DJ2, respectively.

of Figure 11b. It is worth noticing that the units of  $R_s$  and  $r_d$  are  $\Omega\mu\text{m}$  ( $\Omega\mu\text{m}^2$ ) for 2D (3D) junctions, respectively. Once determined the diode equivalent circuit, the cut-off frequency can be defined as the frequency at which  $v^*/j^* = r_d$  :

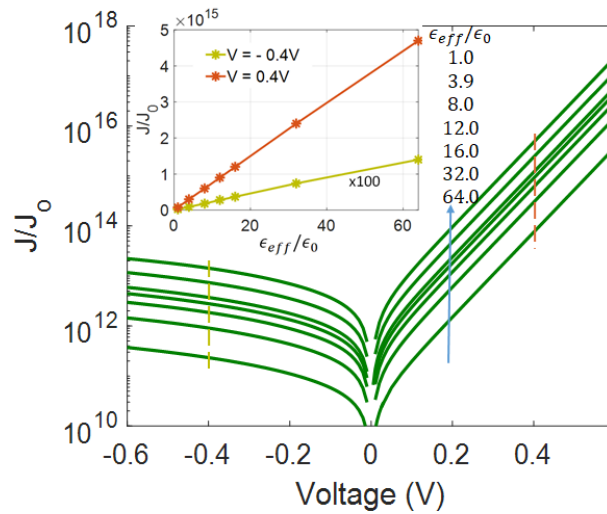
$$f_c = \frac{1}{2\pi C_T(r_d || R_s)} \quad (26)$$

Figure 11a. shows  $f_c$  as a function of the dc voltage for both 2DJ and 3DJ ignoring the extrinsic contact resistance. For the 2D case, we have considered the devices 2DJ1 (small gap) and 2DJ3 (large gap), which have been compared with equivalent 3D devices 3DJ1 and 3DJ2, respectively, in the sense of having again  $(E_F - E_V)|_{2D} = (E_F - E_V)|_{3D} = (E_c - E_F)|_{2D} = (E_c - E_F)|_{3D}$ . At low bias ( $V < 0.4\text{ V}$ ),  $f_c$  exhibits the highest values for both 2D and 3D cases. However in this range of voltages  $r_d \gg R_s$  and  $C_{dp} \gg C_{df}$ , and the cut-off frequency can be approximated as  $f_c \approx 1/2\pi C_{dp} R_s$ . Our simulation shows that the 2DJ1 device, which has the same gap than the 3DJ1 device, exhibits  $f_c$  almost two orders of magnitude less than its 3D counterpart at low bias. By choosing large gap semiconductors like the monolayer  $\text{MoS}_2$  the maximum  $f_c$  can reach the GHz range, although far away from the frequencies reached by 3DJs, as exemplified by the 3DJ2 device.

In Figure 11b we have analyzed the influence of doping in defining  $f_c$ . Specifically, it shows the zero bias cut-off frequency for 2DJ3 and 3DJ2 devices as a function of doping density which has been characterized by  $(E_c - E_F)/kT$ . Given that we have considered symmetrical junctions, then  $(E_F - E_V)|_{p\text{-side}} = (E_c - E_F)|_{n\text{-side}}$ . The results obtained reveal the beneficial effect of high doping to get the highest possible  $f_c$ . According to our numerical result, the silicon based 3DJ can reach zero bias cut-off frequencies over tens of GHz, meanwhile the  $\text{MoS}_2$  based 2DJ can reach  $\sim 1$  GHz. Further investigation will be needed with calibrated parameters to foresee the potential of 2DJs.

## 6. Impact of the surrounding dielectric permittivity

In this section, we have analyzed the impact of the surrounding dielectric medium on the J-V characteristics of 2DJs. Because of the bi-dimensionality they are quite sensitive to the surrounding dielectric, so it is possible to design devices with tailored depletion capacitance (Eq. 18) and current.



**Figure 12.** Impact of the surrounding dielectric permittivity  $\epsilon_{eff}$  on the J-V characteristics of 2DJ.

Eqs. 13 and 15 show how the current driven by R-G processes inside the EDL depend on  $W_{D,eff}$  and the maximum lateral electric field  $F_0$ , which are both dependent on the dielectric constant of the surrounding media. Figure 12 shows the dependence of the relative current density on the effective dielectric constant  $\epsilon_{eff}$  for the symmetric device 2DJ3 described in Table I. We have assumed that the dielectric-semiconductor interface is free of charge density. The inset of Figure 12 shows the dependence of the relative current on  $\epsilon_{eff}$  at both reverse bias and forward bias, exhibiting a linear relationship as predicted by Eqs. 13 and 15, respectively.

## 7. Conclusions

We have investigated the electrostatics and transport properties of 2D lateral pn junctions driven out-of-equilibrium. For a such purpose we have implemented a physics-based simulator where the 2D Poisson's equation is solved self-consistently with the drift-diffusion and continuity equations. Our numerical simulations reveal the impact of R-G processes inside the depletion layer in the J-V characteristics. Deviations from ideal J-V characteristics and the impact of the dimensionality has been thoroughly discussed. We have also discussed the possibility of tuning the J-V characteristics by using the permittivity of the surrounding environment. Moreover, we have analyzed the capacitances and conductance of 2DJs, which allow to define an equivalent circuit. Based on it, we have benchmarked the cut-off frequency of 2DJ for different gaps and doping scenarios, taking the 3DJ case as the reference. The present work opens the door to a wider exploration of potential advantages that 2DJ could bring in terms of FoMs given the long list of available 2D materials. For that to happen a set of material-dependent calibrated parameters is required for any given technology.

## 8. Acknowledgments

This project has received funding from the European Union's Horizon 2020 research and innovation programme under grant agreements No GrapheneCore2 785219 and No GrapheneCore3 881603, from Ministerio de Ciencia, Innovación y Universidades under grant agreement RTI 2018-097876-B-C21(MCIU/AEI/FEDER, UE), and project 001-P-0011702-GraphCAT: Comunitat Emergent de grafè a Catalunya, co-funded by FEDER within the framework of Programa Operatiu FEDER de Catalunya 2014-2020.

# Appendix. Self-consistent algorithm to numerically investigate the 2D lateral pn junction

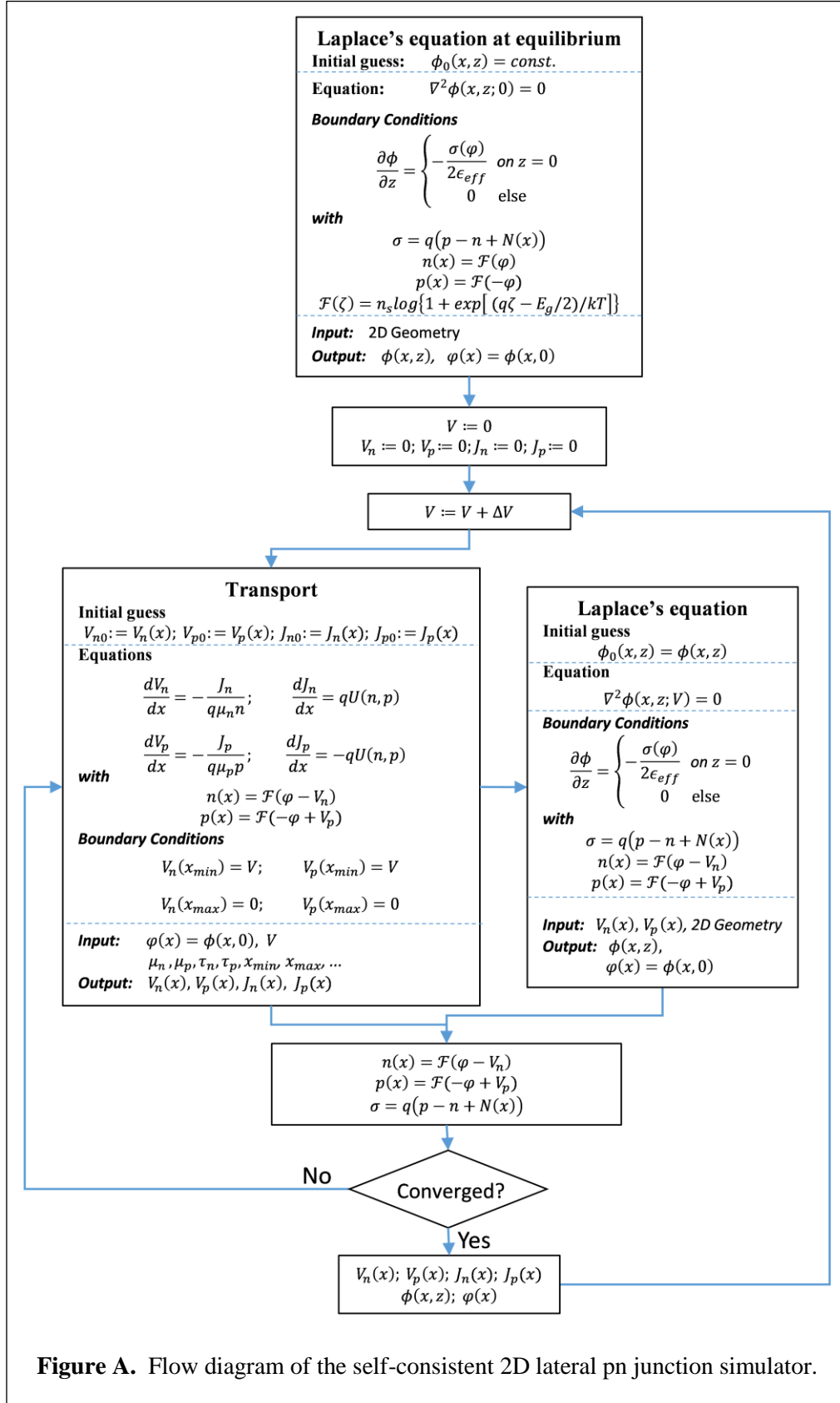


**Figure A.** Flow diagram of the self-consistent 2D lateral pn junction simulator.

As mentioned in the description of the numerical model, we have implemented a self-consistent method in order to solve the system of Eqs. 2-5. Our method follow the steps as presented in the flow diagram of Figure A. For both reverse bias and forward bias the algorithm starts from the solution of the 2D Poisson's equation at thermal equilibrium in the  $x$ - $z$  plane by using an elementary initial guess  $\phi_0(x, z) = \text{const}$ .

To find the solution  $[\varphi_k(x), V_{n,k}(x), V_{p,k}(x), J_{n,k}(x), J_{p,k}(x)]$  to the system of equations at the applied bias  $V_k$ , where  $x \in [x_{min}, x_{max}]$ ,  $l$  iterations are needed before the algorithm converges. In the iteration  $i$  ( $i = 1, 2, 3, \dots, l$ ), firstly, the 1D transport's equations (Drift-Diffusion + Continuity) are solved under the boundary conditions imposed by the quasi-Fermi potentials, to find  $[V_{n,k}^i(x), V_{p,k}^i(x), J_{n,k}^i(x), J_{p,k}^i(x)]$ . In this point, the initial guess is the solution of the previous iteration  $[V_{n,k}^{i-1}(x), V_{p,k}^{i-1}(x), J_{n,k}^{i-1}(x), J_{p,k}^{i-1}(x)]$  and the used electrostatic potential is that from the previous iteration  $\phi_k^{i-1}(x)$ . Secondly, the 2D out-of-equilibrium Laplace's equation is solved in the  $x$ - $z$  plane, under the boundary conditions given in Fig. 2, to find  $\phi_k(x, z)$ . At this point, the initial guess is the electrostatic potential  $\phi_k^{i-1}(x, z)$  found in the previous iteration and the quasi-Fermi potentials are those from the present iteration  $V_{n,k}^i(x), V_{p,k}^i(x)$ . Then, the sheet charge density distribution  $\sigma_k^i(x)$  is calculated with the new solution  $[\varphi_k(x), V_{n,k}(x), V_{p,k}(x)]$  and compared with the sheet charge density distribution  $\sigma_k^{i-1}(x)$  of the previous iteration by means of the relative error defined as:

$$\varepsilon_k^i = \left\{ \frac{\int_{x_{min}}^{x_{max}} [\sigma_k^i(x) - \sigma_k^{i-1}(x)]^2 dx}{\int_{x_{min}}^{x_{max}} [\sigma_k^{i-1}(x)]^2 dx} \right\}^{1/2}$$

When the algorithm converges for the bias  $V_k$ , the solution  $[\varphi_k(x), V_{n,k}(x), V_{p,k}(x), J_{n,k}(x), J_{p,k}(x)]$  serves as the initial guess for the first iteration of the self-consistency at bias  $V_{k+1}$ . This way, the algorithm is able to find the 2D electrostatic potential  $\phi(x, z)$ , the 1D electrostatic potential  $\varphi(x) = \phi(x, 0)$ , the quasi-Fermi potentials  $V_n(x)$  and  $V_p(x)$ , the density currents  $J_n(x)$  and  $J_p(x)$ , and the total current  $J = J_n(x_o) + J_p(x_o)$ , for any given bias point. Here,  $x_o$  is any point belonging to the interval  $[x_{min}, x_{max}]$ .

## REFERENCES

- [1] B. Radisavljevic, A. Radenovic, J. Brivio, V. Giacometti, and A. Kis, "Single-layer MoS2 transistors," Nature Nanotechnology 6, 147-150 (2011).
- [2] F. Schwierz, J. Pezoldt, and R. Granzner, "Two-dimensional materials and their prospects in transistor electronics," Nanoscale 7, 8261-8283 (2015).
- [3] A. Singh, A. Uddin, T. Sudarshan, and G. Koley, "Tunable reverse-biased graphene/silicon heterojunction Schottky diode sensor.," Small 10 1555–1565 (2014).
- [4] H. Yang et al., "Graphene Barristor, a Triode Device with a Gate-Controlled Schottky Barrier," Science 336, 1140–1143 (2012).
- [5] M. S. Choi et al., "Lateral MoS2 p-n junction formed by chemical doping for use in high-performance optoelectronics," ACS Nano 8, 9332–9340 (2014).
- [6] C. H. Lee et al., "Atomically thin p-n junctions with van der Waals heterointerfaces," Nature

- Nanotechnology 9, 676-681 (2014).
- [7] F. A. Chaves, D. Jiménez, J. E. Santos, P. Bøggild, and J. M. Caridad, “Electrostatics of metal–graphene interfaces: sharp p–n junctions for electron-optical applications,” *Nanoscale* 11, 10273–10281 (2019).
- [8] D. Li et al., “Two-dimensional non-volatile programmable p-n junctions,” *Nature Nanotechnology* 12, 901–906, 2017.
- [9] R. Frisenda, A. J. Molina-Mendoza, T. Mueller, A. Castellanos-Gomez, and H. S. J. Van Der Zant, “Atomically thin p-n junctions based on two-dimensional materials”, *Chem. Soc.* 47, 3339–3358 (2018).
- [10] D. Jariwala, A. R. Davoyan, J. Wong, and H. A. Atwater, “Van der Waals Materials for Atomically-Thin Photovoltaics: Promise and Outlook,” *ACS Photonics* 4, 2962-2970 (2017).
- [11] M. Y. Li et al., “Epitaxial growth of a monolayer WSe<sub>2</sub>-MoS<sub>2</sub> lateral p-n junction with an atomically sharp interface,” *Science* 349, 524-528 (2015).
- [12] M. L. Tsai et al., “Single Atomically Sharp Lateral Monolayer p-n Heterojunction Solar Cells with Extraordinarily High Power Conversion Efficiency,” *Adv. Mater.* 29, 1701168 (2017).
- [13] J. Cheng, C. Wang, X. Zou, and L. Liao, “Recent Advances in Optoelectronic Devices Based on 2D Materials and Their Heterostructures,” *Adv. Opt. Mater.* 7, 1800441 (2019).
- [14] F. A. Chaves and D. Jiménez, “Electrostatics of two-dimensional lateral junctions” *Nanotechnology* 29, 275203 (2018).
- [15] A. S. Achoyan, A. É. Yesayan, É. M. Kazaryan, and S. G. Petrosyan, “Two-dimensional p-n junction under equilibrium conditions,” *Semiconductors* 36, 903–907 (2002).
- [16] Y. G. Peisakhovich, A. A. Shtygashev, L. A. Borynyak, and N. Y. Petrov, “Electric field and charge density in the plane of a quasi-equilibrium asymmetric 2D p–n junction with zero current,” *Tech. Phys.* 60, 1494–1500 (2015).
- [17] A. Nipane, S. Jayanti, A. Borah, and J. T. Teherani, “Electrostatics of lateral p-n junctions in atomically thin materials,” *J. Appl. Phys.* 122, 194501 (2017).
- [18] N. Ma and D. Jena, “Carrier statistics and quantum capacitance effects on mobility extraction in two-dimensional crystal semiconductor field-effect transistors,” *2D Materials* 2, 015003 (2015).
- [19] Y. Taur and T. H. Ning, *Fundamentals of Modern VLSI Devices*. 2009.
- [20] S. M. Sze and K. K. Ng, “Physics of Semiconductor Devices, 3rd Edition - Simon M. Sze, Kwok K. Ng,” *Phys. Semicond. Devices, 3rd Ed. John Wiley Sons, Inc.; NJ*, 2007.
- [21] M. Shur, “Physics of Semiconductor Devices,” *Prentice-Hall Englewood Cliffs, New Jersey*, 1990.
- [22] B. W. H. Baugher, H. O. H. Churchill, Y. Yang, and P. Jarillo-Herrero, “Optoelectronic devices based on electrically tunable p-n diodes in a monolayer dichalcogenide,” *Nature Nanotechnology* 9, 262-267 (2014).